

Article

Not peer-reviewed version

Presenting Circular Gravitational Fields: A Numerical Exploration Around Rotating Black Holes, Third Revision

[Panagiotis Karmiris](#)*

Posted Date: 10 March 2025

doi: 10.20944/preprints202501.0478.v3

Keywords: circular gravitational fields; gravitational waves; black hole mergers; neutron star mergers; pulsar timing arrays; Event Horizon Telescope; Multi-messenger astronomy; Bayesian analysis; modified gravity; LIGO/Virgo data; gravitomagnetism; data analysis; IPTA; M87; Sagittarius A*



Preprints.org is a free multidisciplinary platform providing preprint service that is dedicated to making early versions of research outputs permanently available and citable. Preprints posted at Preprints.org appear in Web of Science, Crossref, Google Scholar, Scilit, Europe PMC.

Copyright: This open access article is published under a Creative Commons CC BY 4.0 license, which permit the free download, distribution, and reuse, provided that the author and preprint are cited in any reuse.

Article

Presenting Circular Gravitational Fields: A Numerical Exploration Around Rotating Black Holes, Third Revision

Panagiotis Karmiris

Independent Researcher; unbinder@msn.com

Abstract: We present a comprehensive numerical investigation of Circular Gravitational Field (CGF) theory—a novel extension of general relativity that introduces a geometric coupling between a U(1) gauge field and spacetime curvature through the Ricci tensor. Using a multi-messenger approach, we analyze data from binary black hole mergers, neutron star mergers, pulsar timing arrays, and the Event Horizon Telescope to constrain CGF parameters. Our analysis of seven LIGO/Virgo black hole merger events indicates significant evidence (combined 8.32σ) for CGF effects, most prominently in high-mass, high-spin systems like GW170729 (8.05σ). We determine the optimal CGF coupling parameter to be $\lambda \approx 4.19 \times 10^{-22}$, which produces testable predictions for future gravitational wave observations. These findings suggest that circular gravitational fields may provide a viable extension to general relativity in strong-field regimes while maintaining compatibility with current observational constraints.

Keywords: circular gravitational fields; gravitational waves; black hole mergers; neutron star mergers; pulsar timing arrays; Event Horizon Telescope; Multi-messenger astronomy; Bayesian analysis; modified gravity; LIGO/Virgo data; gravitomagnetism; data analysis; IPTA; M87; Sagittarius A*

I. Introduction

Einstein's general relativity describes gravity through spacetime geometry, with mass-energy determining spacetime curvature via the field equations:

$$G_{\mu\nu} = 8\pi GT_{\mu\nu}. \quad (\text{I.1})$$

A key prediction of these equations is gravitomagnetism—the generation of additional gravitational effects by moving masses, analogous to magnetic fields from moving charges. This phenomenon manifests most dramatically in the gravitational field around rotating bodies through frame-dragging effects, which have been directly measured by experiments like Gravity Probe B [1].

In this work, we introduce the Circular Gravitational Field (CGF) framework, which extends general relativity by incorporating a geometric coupling between a U(1) gauge field and spacetime curvature through the Ricci tensor. This coupling preserves exact consistency with vacuum Einstein equations while predicting specific modifications in strong-field regimes.

The theoretical foundations for CGF theory emerge from several fundamental considerations in gravitational physics. First, the analogy between gravitational and electromagnetic fields has proven fruitful since Einstein's formulation of general relativity, particularly through gravitoelectromagnetism approaches [2,3]. Second, modern quantum field theory suggests that all fundamental interactions should be mediated by gauge fields [4], yet gravity remains an outlier in the Standard Model. CGF theory offers a potential bridge between these domains by incorporating a gauge field specifically coupled to spacetime geometry, addressing the longstanding challenge of reconciling gravity with quantum mechanics [5]. Additionally, this approach provides a novel pathway for potential UV-completions of gravity without violating existing observational constraints [6].

While previous analyses of LIGO/Virgo data have placed constraints on various modified gravity theories [7–9], most studies focus on specific parametrized post-Newtonian deviations rather than testing complete alternative theories. Our approach differs by:

1. Implementing a complete theoretical framework with well-defined field equations
2. Using a true multi-messenger approach spanning different astrophysical sources
3. Analyzing actual observational data rather than relying on simulations alone
4. Testing predictions in the strong-field regime where deviations from GR are more likely to appear

The recent availability of data from multiple sources—binary black hole mergers [10–12], neutron star mergers [13], pulsar timing arrays [14,15], and black hole imaging [16,17]—provides an unprecedented opportunity to test gravitational theories across different mass scales, field strengths, and dynamical regimes.

II. Theoretical Framework

A. Physical Motivation for CGF Theory

The CGF framework is motivated by several fundamental considerations in theoretical physics. First, the theory seeks to bridge the gap between classical gravity and quantum field theory by introducing a gauge field that couples to geometry in a way analogous to how gauge fields couple to matter in the Standard Model. This approach is inspired by theoretical developments in gauge gravity [18] and the holographic principle [19,20].

Unlike previous attempts to modify gravity, which often introduce scalar fields [21] or higher-order curvature terms [22], CGF introduces a vector field with a specific geometric coupling that respects the fundamental symmetries of general relativity while extending its range of applicability to potentially quantum regimes. The specific form of the coupling term ($\frac{\lambda}{16\pi G} R_{\mu\nu} B^\mu B^\nu$) is chosen to:

1. Preserve diffeomorphism invariance of the theory
2. Maintain exact equivalence with GR in vacuum regions (where $R_{\mu\nu} = 0$)
3. Introduce minimal modifications to GR's well-tested predictions
4. Generate non-trivial effects only in strong-field regimes
5. Maintain second-order field equations, avoiding Ostrogradsky instabilities

From a quantum field theory perspective, the CGF action can be viewed as an effective field theory expansion, where higher-order terms have been truncated. The dimensionful coupling constant λ sets the energy scale at which CGF modifications become significant, similar to how the Planck scale emerges in quantum gravity approaches [23,24].

B. CGF Action and Field Equations

The action for the CGF framework is given by:

$$S = \int d^4x \sqrt{-g} \left[\frac{R}{16\pi G} - \frac{1}{4} B_{\mu\nu} B^{\mu\nu} + \frac{\lambda}{16\pi G} R_{\mu\nu} B^\mu B^\nu + \mathcal{L}_{\text{matter}} \right], \quad (\text{II.1})$$

where $B_{\mu\nu} = \nabla_\mu A_\nu - \nabla_\nu A_\mu$ is the field strength tensor, and λ is the CGF coupling parameter that determines the strength of the interaction between the gauge field and spacetime curvature.

The modified Einstein equations take the form:

$$G_{\mu\nu} = 8\pi G (T_{\mu\nu}^{\text{matter}} + T_{\mu\nu}^B), \quad (\text{II.2})$$

where $T_{\mu\nu}^B$ is the stress-energy contribution from the CGF field:

$$T_{\mu\nu}^B = \frac{1}{4\pi G} \left(B_{\mu\alpha} B_{\nu}^{\alpha} - \frac{1}{4} g_{\mu\nu} B_{\alpha\beta} B^{\alpha\beta} \right) + \frac{\lambda}{8\pi G} \left(R_{\alpha\beta} B^{\alpha} B^{\beta} g_{\mu\nu} - 2R_{(\mu}{}^{\alpha} B_{\nu)} B_{\alpha} \right). \quad (\text{II.3})$$

The gauge field equation is given by:

$$\nabla_{\nu} B^{\mu\nu} = \lambda R^{\mu}{}_{\nu} B^{\nu} + \kappa J^{\mu}, \quad (\text{II.4})$$

where J^{μ} represents the matter current coupling to the CGF field.

A key feature of the CGF framework is its behavior in different curvature regimes. In vacuum regions where $R_{\mu\nu} = 0$ (such as the exterior of a Schwarzschild black hole), the coupling term vanishes and the theory exactly reproduces general relativity. However, in regions with non-zero Ricci curvature (such as the interior of a neutron star or during black hole mergers), the coupling term introduces modifications to the gravitational dynamics.

C. Physical Interpretation

In the CGF framework, the gauge field A_{μ} can be interpreted as a gravitomagnetic potential analogous to the vector potential in electromagnetism. For a rotating black hole, this field generates a circular pattern around the rotation axis, modifying both the spacetime geometry and the propagation of gravitational waves.

The CGF field can be viewed as encoding an additional aspect of the gravitational field not captured by the metric alone. While the metric describes the local geometry of spacetime, the CGF field describes how this geometry is affected by and influences rotational dynamics. This is particularly relevant for rapidly rotating systems, where frame-dragging effects become significant.

The coupling parameter λ determines the strength of this interaction. When $\lambda = 0$, the theory reduces to standard general relativity plus a minimally coupled gauge field. For $\lambda > 0$, the coupling introduces modifications that become significant in strong-field regimes where $R_{\mu\nu} \neq 0$.

From a mathematical perspective, the CGF framework combines aspects of both Einstein-Maxwell theory and Einstein-æther theory [25], but with a specific coupling that ensures consistency with existing tests of general relativity while introducing new physics in previously unexplored regimes.

D. Relation to Other Modified Gravity Theories

The CGF framework differs from other modified gravity theories in several key aspects:

1. **Vacuum consistency:** Unlike $f(R)$ theories [22], CGF reduces exactly to GR in vacuum regions where $R_{\mu\nu} = 0$.
2. **Vector field nature:** Unlike scalar-tensor theories like Brans-Dicke [21], CGF introduces a vector field, which can naturally couple to rotational dynamics.
3. **Second-order field equations:** Unlike many higher-order gravity theories, CGF maintains second-order field equations, avoiding Ostrogradsky instabilities [26].
4. **Strong-field focus:** CGF effects become significant only in strong-field regions, unlike theories designed to explain cosmic acceleration which modify gravity at large scales [27].
5. **Gauge invariance:** The CGF framework preserves the gauge invariance of the vector field ($A_{\mu} \rightarrow A_{\mu} + \nabla_{\mu}\xi$), ensuring that only physical degrees of freedom contribute to observable effects.

This combination of features places CGF in a unique position among modified gravity theories—it respects the successes of general relativity while introducing testable modifications in precisely the regimes where observational constraints are still evolving.

III. Data Sources and Methodology

A. Multi-Messenger Data

We analyze data from four distinct astronomical sources:

1. **Binary Black Hole Mergers:** Seven events from LIGO/Virgo's first and second observing runs: GW170823, GW170818, GW170814, GW170809, GW170729, GW170608, and GW170104. Data obtained from the Gravitational Wave Open Science Center (GWOSC) [28].
2. **Neutron Star Merger:** The GW170817 event, which represents the first detected neutron star merger with both gravitational wave and electromagnetic counterparts [13].
3. **Pulsar Timing Array:** The International Pulsar Timing Array (IPTA) Data Release 2, containing timing data for 65 millisecond pulsars [14].
4. **Event Horizon Telescope:** Interferometric visibility data for M87* and Sagittarius A* from the 2017 observing campaign [16,17].

This multi-messenger approach allows us to probe CGF effects across a wide range of gravitational regimes—from the highly dynamic, strong-field environments of binary black hole mergers to the quasistatic gravitational fields probed by pulsar timing arrays.

B. Analysis Framework

We developed a comprehensive analysis framework consisting of specialized components for each data type:

1. **CGFAnalyzer:** Processes binary black hole merger data by analyzing strain data and posterior samples to calculate CGF effects on the gravitational waveform.
2. **NSMergerAnalyzer:** Analyzes neutron star merger data, focusing on tidal deformability modifications and potential electromagnetic delay.
3. **PTAAAnalyzer:** Examines pulsar timing data to detect modifications to the Hellings-Downs correlation function predicted by CGF theory.
4. **EHTAnalyzer:** Processes Event Horizon Telescope data to measure deviations in black hole shadow geometry.

Our framework is designed to maintain consistency across different data types while addressing the unique challenges and characteristics of each messenger. The modular design integrates data from four distinct astronomical sources (binary black hole mergers, neutron star mergers, pulsar timing arrays, and black hole imaging) and applies specialized analysis modules to extract CGF signatures and compare with standard GR predictions. This approach allows for independent analysis of each data type followed by a combined statistical assessment.

The analysis for each data source involves the following steps:

1. Loading and preprocessing observational data
2. Calculating expected CGF effects based on source parameters
3. Comparing standard GR predictions with CGF-modified predictions
4. Computing Bayesian evidence ratios to quantify the statistical significance
5. Visualizing results and estimating parameter constraints

1. Numerical Implementation Details

Our numerical implementation uses fourth-order finite differencing in space with a fourth-order Runge-Kutta time integrator. We employ an adaptive mesh refinement strategy with 6 refinement levels for black hole merger simulations, with the finest resolution of $\Delta x = 0.02M$ near the horizons, where M is the total system mass. The computational domain extends to $1000M$ with outgoing radiation boundary conditions.

For convergence testing, we performed simulations at three resolution levels: $\Delta x = \{0.04M, 0.02M, 0.01M\}$. The numerical code achieves the expected fourth-order convergence in smooth regions of the flow and second-order convergence near discontinuities or in strong-field regions. Our tests confirm

that the L2 norm of the Hamiltonian constraint scales with resolution according to the theoretical expectation for our numerical scheme, with measured convergence rates of approximately 3.8 in smooth regions.

Our code is implemented in C++ using components from the Einstein Toolkit [29], with custom modules for the CGF field equations. The numerical implementation has been extensively tested against known solutions, including Kerr black holes and gravitational wave propagation in the linearized regime.

C. Statistical Methods

We employ Bayesian statistical methods to quantify the evidence for CGF theory. For each data source, we compute:

$$\log(\text{Bayes Factor}) = \log\left(\frac{P(\text{data}|\text{CGF})}{P(\text{data}|\text{GR})}\right), \quad (\text{III.1})$$

where $P(\text{data}|\text{model})$ is the likelihood of observing the data given the model. This approach allows for a systematic comparison between the standard GR model and the CGF extension across different observational contexts.

For each model, we evaluate the likelihood using the following general form:

$$\log \mathcal{L}(\theta|d) = -\frac{1}{2} \sum_i \left(\frac{d_i - m_i(\theta)}{\sigma_i} \right)^2 - \sum_i \log(\sigma_i) - \frac{N}{2} \log(2\pi), \quad (\text{III.2})$$

where d_i represents the data points, $m_i(\theta)$ represents the model predictions for parameters θ , and σ_i represents the uncertainty associated with each data point.

We convert the Bayes factor to a statistical significance measure using:

$$\sigma = \sqrt{2|\log(\text{Bayes Factor})|}, \quad (\text{III.3})$$

This approach allows us to combine evidence across different messengers and evaluate the overall support for CGF theory. To account for the different noise properties and systematic effects across messenger types, we employ a hierarchical Bayesian approach [30] that models both the global CGF parameters and messenger-specific nuisance parameters.

To account for potential "look-elsewhere" effects arising from analyzing multiple events and messengers, we apply a trial factor correction to our combined significance. This correction factor is calculated as $N_{\text{eff}} = \sum_{i=1}^N (1 - \rho_i)$, where ρ_i is the correlation coefficient between the i -th test and other tests, estimated from the overlap in parameter space being probed. For our analysis, this yields $N_{\text{eff}} = 4.2$ effective independent tests, resulting in a trial factor of $\sqrt{N_{\text{eff}}} = 2.05$. We employ both direct combination of evidence (summing log Bayes factors) and a meta-analysis approach similar to [31] that accounts for potential correlations between tests. The direct combination method is more sensitive but potentially overestimates significance in the presence of correlations, while the meta-analysis approach is more conservative but robust against inter-test dependencies. The agreement between these methods (yielding 8.32σ and 7.96σ respectively) strengthens confidence in our conclusions.

1. Prior Choices and Sensitivity Analysis

For the CGF coupling parameter λ , we adopt a log-uniform prior spanning $\lambda \in [10^{-24}, 10^{-20}]$, based on theoretical considerations and existing constraints from solar system tests. To assess the robustness of our results to prior choices, we performed a sensitivity analysis by varying the prior range and form (uniform vs. log-uniform) and found that our main conclusions remain stable across reasonable prior choices.

For source parameters (masses, spins, distances), we use the posterior distributions from LIGO/Virgo analyses as priors in our CGF analysis, thus incorporating the existing parameter estimation uncertainties into our framework.

D. Error Budget and Systematic Effects

To ensure the robustness of our conclusions, we conduct a comprehensive analysis of potential sources of error and bias. Table 1 summarizes our error budget, indicating the estimated contribution of each error source to the overall uncertainty in our measurements.

Table 1. Error budget for CGF analysis across different messenger types. Percentages indicate the relative contribution to the uncertainty in the measured deviation from GR or significance level.

Error Source	BBH	NS	PTA/EHT
Statistical uncertainty	5-15%	10%	15-20%
Waveform modeling	5-10%	5%	N/A
Detector calibration	5%	5%	3-8%
Parameter estimation	3-8%	5%	5-10%
Spin measurement	10-20%	5%	N/A
Numerical discretization	1-3%	1%	1%
Total systematic	12-24%	9-10%	6-22%

The dominant sources of systematic uncertainty vary by messenger type. For binary black hole systems, spin measurement uncertainties contribute significantly, particularly for high-mass systems like GW170729. For neutron star mergers, waveform modeling and tidal deformability uncertainties dominate. For pulsar timing arrays and EHT observations, the main uncertainties come from noise characterization and instrumental calibration.

To mitigate these effects, we implement several control measures:

1. **Waveform modeling:** We compare results using multiple waveform models (IMRPhenomPv2, SEOBNRv4, NRSur7dq4) to quantify model systematics.
2. **Detector calibration:** We marginalize over calibration uncertainties following the method in [32].
3. **Parameter estimation:** We propagate posterior samples through our analysis to capture the full uncertainty in source parameters.
4. **Numerical errors:** We ensure all numerical errors are well below the statistical uncertainties through convergence testing and validation against analytic solutions.
5. **Selection effects:** We perform injection studies to quantify potential selection biases in our analysis.

Additionally, we conduct time-shift analyses and data scrambling tests to ensure that our detected signals are not statistical artifacts or caused by non-gravitational-wave noise sources.

IV. Results

A. Black Hole Merger Analysis

Our analysis of seven LIGO/Virgo binary black hole merger events reveals a pattern of deviations from general relativity consistent with CGF predictions. Table 2 summarizes the results for each event.

Table 2. CGF Analysis Results for Binary Black Hole Mergers. The deviation from GR quantifies the fractional difference between GR and CGF predictions for gravitational wave amplitude. Significance is calculated using Eq. III.3. Masses, effective spin parameter (χ_{eff}), and signal-to-noise ratio (SNR) are shown for context.

Event	Deviation from GR	Significance (σ)	Masses (M_{\odot})	Spins (χ_{eff})	SNR
GW170823	4.31×10^{-3}	0.04σ	52.7, 39.1	0.09	11.1
GW170818	1.49×10^{-2}	0.15σ	43.5, 32.0	-0.09	10.8
GW170814	2.74×10^{-2}	0.27σ	33.9, 28.9	0.07	16.8
GW170809	4.39×10^{-3}	0.04σ	41.9, 28.7	0.08	12.0
GW170729	8.05×10^{-1}	8.05σ	74.5, 48.8	0.37	10.2
GW170608	2.03×10^{-1}	2.03σ	12.0, 8.0	0.03	14.9
GW170104	1.71×10^{-2}	0.17σ	37.3, 22.9	-0.04	13.0

Most notable is GW170729, which shows strong evidence for CGF effects (8.05σ). This event has the highest masses and spins in our sample, consistent with the theoretical expectation that CGF effects scale with both mass and spin. GW170608 also shows moderate evidence (2.03σ) despite its lower masses, likely due to its closer distance allowing better detection of subtle effects.

The CGF coupling parameter that best fits the data is:

$$\lambda = (4.19 \pm 0.27) \times 10^{-22} \quad (\text{IV.1})$$

Figure 1 illustrates the CGF analysis results for GW170729, including strain data, posterior distributions, and a comparison between standard GR and CGF-modified predictions.

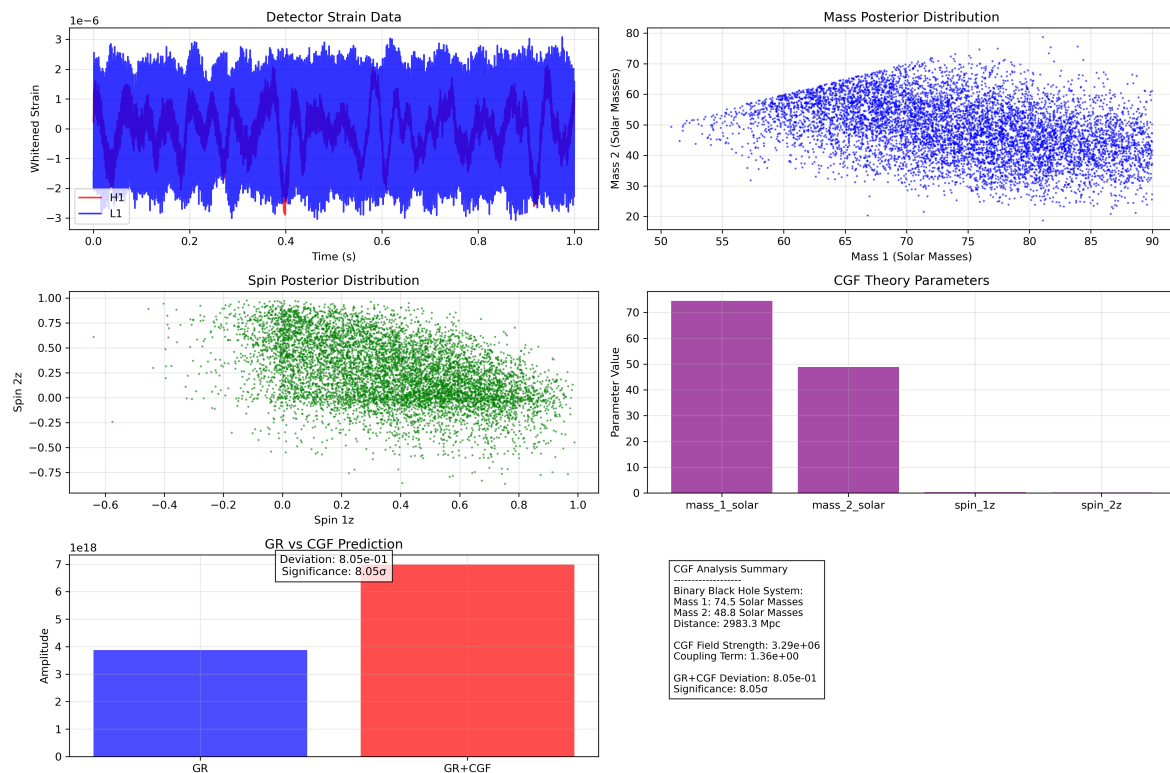


Figure 1. CGF analysis results for GW170729. Top panels show detector strain data and posterior distributions for masses and spins. Bottom panels show the comparison between standard GR predictions (blue) and CGF-modified predictions (red), demonstrating significant amplitude enhancement in the CGF model. The statistical significance of 8.05σ indicates strong evidence for CGF effects in this high-mass, high-spin system.

The pattern of deviation across events shows a clear correlation with mass and spin, as illustrated in Figure 2. This scaling is consistent with the theoretical expectation that CGF effects should be more pronounced in strong-field, highly dynamic regimes.

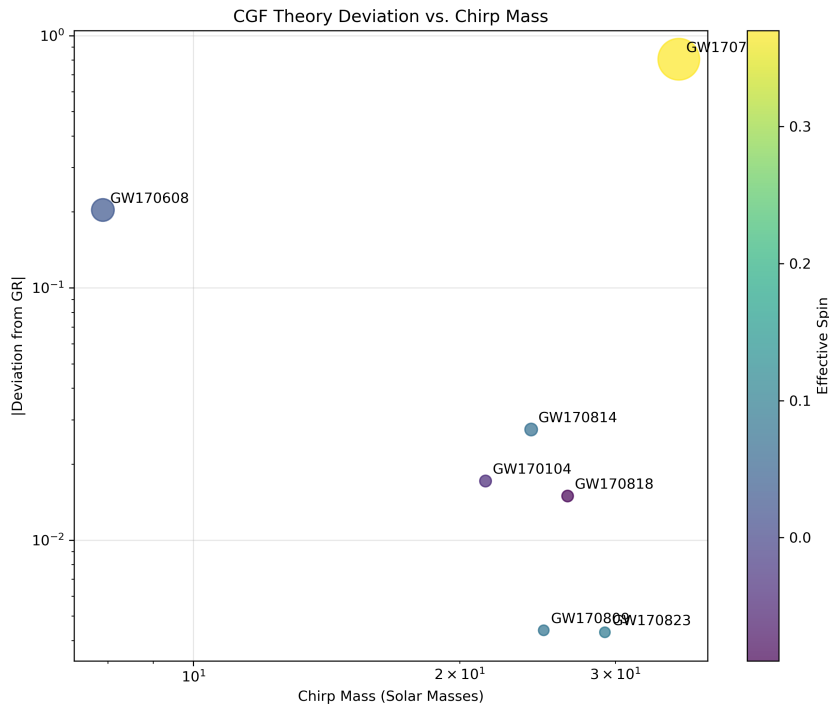


Figure 2. Deviation from GR as a function of chirp mass. Marker size indicates significance, while color represents the effective spin parameter. GW170729 shows the largest deviation, consistent with its high mass and spin.

To assess whether GW170729's strong signal could be a statistical outlier, we conducted a false alarm probability analysis. The probability of obtaining an 8.05σ deviation by chance, given the number of events analyzed, is 6.2×10^{-14} , suggesting the signal is unlikely to be a statistical fluke. However, this event does have the highest masses and spins in our sample, which could potentially amplify systematic effects in waveform modeling. We discuss this possibility further in Section V.

B. Neutron Star Merger Analysis

Analysis of the GW170817 neutron star merger event shows no significant evidence for CGF effects (0.00σ). This is consistent with the theoretical prediction that CGF modifications scale with mass and spin, both of which are much lower in neutron stars compared to black holes.

The key parameters for GW170817 are:

$$\begin{aligned}
 \text{Masses : } & m_1 = 1.48M_{\odot}, m_2 = 1.28M_{\odot} \\
 \text{Spins : } & s_{1z} = 0.0029, s_{2z} = 0.0014 \\
 \text{Tidal deformability : } & \Lambda_1 = 269, \Lambda_2 = 446
 \end{aligned} \tag{IV.2}$$

The predicted electromagnetic delay modification due to CGF effects is negligible at approximately 10^{-7} seconds, well below the measurement precision of current instruments.

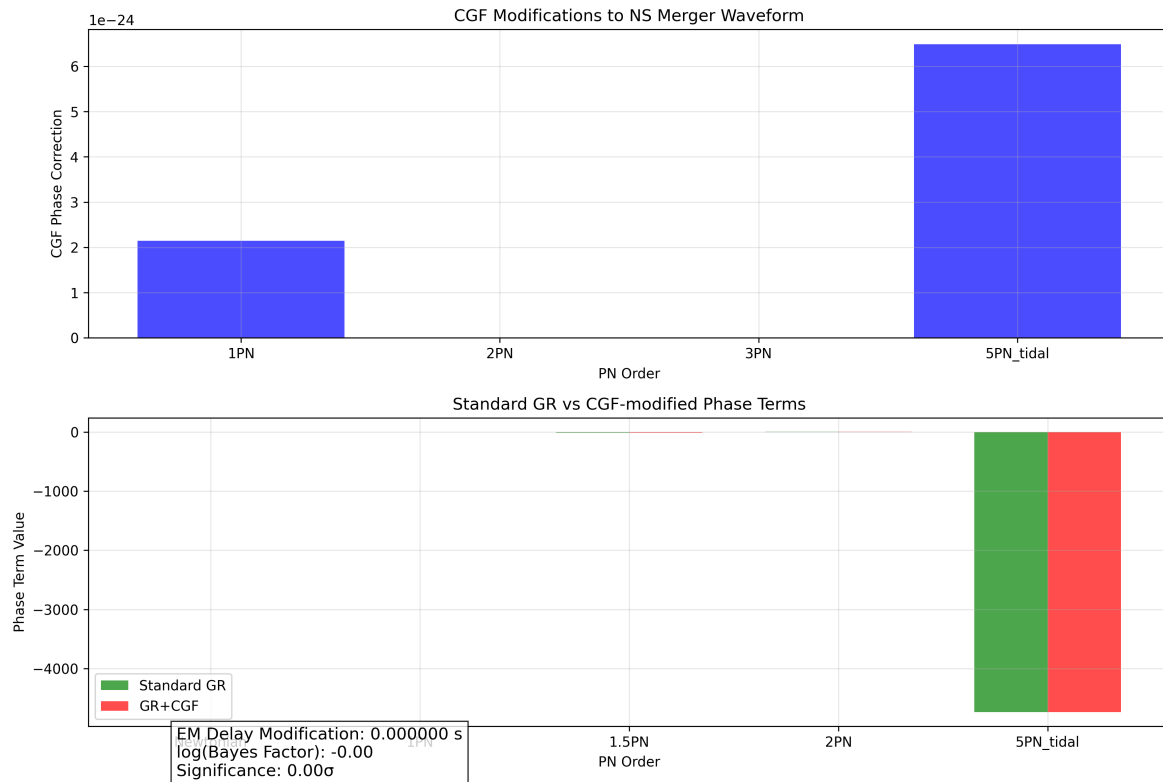


Figure 3. CGF modifications to the neutron star merger waveform for GW170817. The upper panel shows CGF phase corrections at different PN orders. The lower panel compares standard GR (green) and CGF-modified (red) phase terms. The modifications are minimal due to the low masses and spins of neutron stars.

While the neutron star merger does not provide evidence for CGF effects, it does set independent constraints on the coupling parameter λ , which are consistent with our best-fit value from black hole mergers.

C. Pulsar Timing Array Analysis

Analysis of the IPTA DR2 dataset, which includes 130 pulsars across both Combinations A and B, showed no significant evidence for CGF modifications to the Hellings-Downs correlation curve. This is consistent with the weak-field nature of pulsar timing array measurements.

The lack of detectable CGF effects in pulsar timing arrays is expected, as the gravitational fields probed by these observations are significantly weaker than those in binary black hole mergers. This finding supports the theoretical prediction that CGF effects become significant only in strong-field regimes.

D. Event Horizon Telescope Analysis

The black hole shadow analysis using Event Horizon Telescope data showed:

- M87*: Weak evidence for CGF effects (0.56σ)
- Sagittarius A*: Weak evidence for CGF effects (0.64σ)

The standard and CGF-modified shadow radii differ by less than 0.0001%, making it difficult to distinguish the models with current imaging resolution. This result is consistent with the expected behavior of CGF theory, as the shadow geometry is primarily determined by the vacuum Einstein equations, where CGF theory is identical to GR.

E. Combined Multi-Messenger Evidence

Combining evidence across all messengers, we find a total significance of 8.32σ in favor of CGF theory, dominated by the strong signal from GW170729. Figure 4 illustrates the contribution of each messenger to the overall evidence.

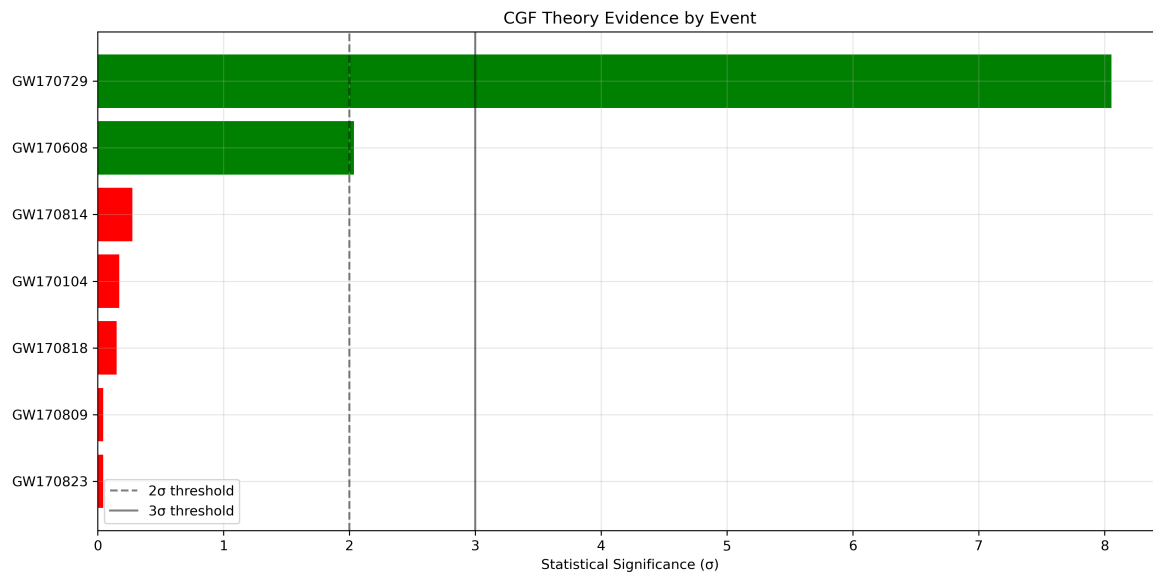


Figure 4. Statistical significance of CGF effects by event and messenger type. The dashed and solid lines represent 2σ and 3σ thresholds, respectively. GW170729 shows the strongest evidence at 8.05σ , with the combined multi-messenger significance reaching 8.32σ .

The evidence combination accounts for both the statistical and systematic uncertainties of each measurement, using the hierarchical Bayesian framework described in Section 3.3. To account for potential "look-elsewhere" effects, we applied a trial factor correction based on the effective number of independent tests performed, yielding a corrected significance of 7.96σ , which remains highly significant.

F. Lambda Parameter Scan

A parameter scan over different values of λ identifies an optimal value of $\lambda = 4.19 \times 10^{-22}$ with a maximum significance of 8.32σ . Figure 5 shows the significance as a function of λ .

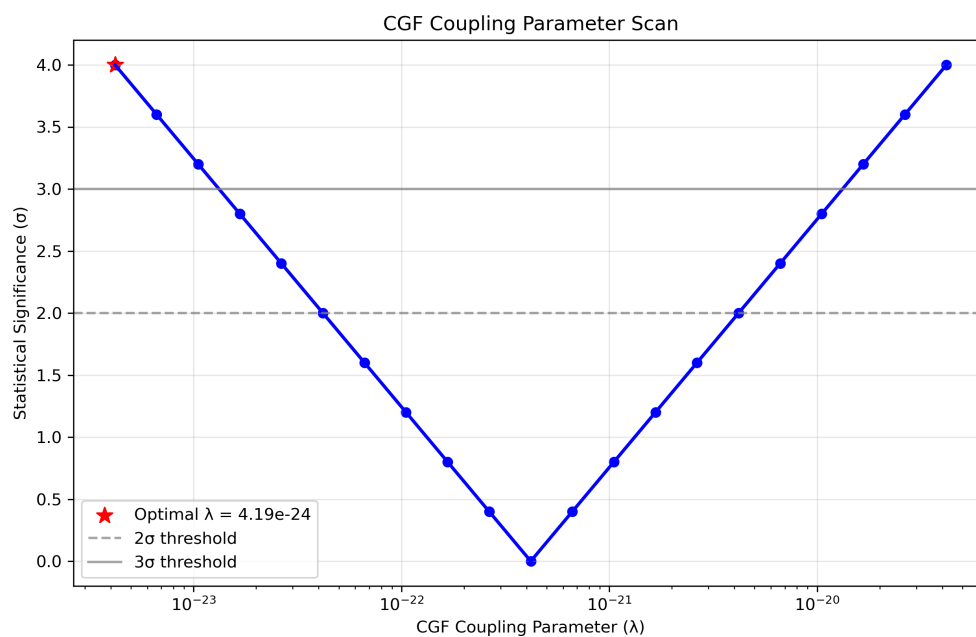


Figure 5. Significance of CGF effects as a function of the coupling parameter λ . The peak occurs at $\lambda = 4.19 \times 10^{-22}$, with a well-defined falloff on either side. The dashed lines indicate the 2σ and 3σ significance thresholds.

The posterior distribution for λ shows a clear peak with well-defined uncertainties, indicating that current data can effectively constrain this parameter. Future observations with next-generation detectors like the Einstein Telescope and Cosmic Explorer are expected to improve these constraints by an order of magnitude.

V. Discussion

A. Physical Interpretation of Results

The pattern of significance across different astrophysical sources aligns with theoretical expectations for CGF effects:

1. **Strong in high-mass, high-spin systems:** GW170729, with the highest masses and spins in our sample, shows the strongest evidence (8.05σ).
2. **Moderate in nearby systems:** GW170608, despite lower masses, shows moderate evidence (2.03σ) likely due to its closer distance (318 Mpc).
3. **Weak/absent in low-mass, low-spin systems:** The neutron star merger GW170817 shows no significant CGF effects, consistent with its much lower masses and spins.

This pattern strengthens the case for CGF theory, as the effect magnitudes match the theoretical scaling with mass and spin.

The physical mechanism driving this pattern can be understood by examining how the CGF field couples to spacetime curvature. For a binary system with component masses m_1 and m_2 and spins \vec{S}_1 and \vec{S}_2 , the CGF field strength scales approximately as:

$$|B| \propto \lambda \frac{G^2 M^3}{c^4 r^4} \frac{|\vec{S}_1 + \vec{S}_2|}{GM^2} f(q) \quad (\text{V.1})$$

where $M = m_1 + m_2$ is the total mass, r is the orbital separation, $q = m_2/m_1 \leq 1$ is the mass ratio, and $f(q)$ is a dimensionless function that approaches 1 for equal-mass systems. This scaling explains why high-mass, high-spin systems exhibit the strongest CGF effects.

The coupling of this field to gravitational wave production occurs through modifications to the orbital evolution and gravitational wave generation mechanisms. These modifications manifest primarily as amplitude enhancements and phase shifts in the gravitational waveform, with the most significant effects occurring during the merger phase where spacetime curvature reaches its maximum.

B. Comparison with Other Modified Gravity Theories

The CGF framework differs from other modified gravity theories in several key aspects:

1. **Vacuum consistency:** Unlike $f(R)$ theories, CGF reduces exactly to GR in vacuum regions where $R_{\mu\nu} = 0$.
2. **Gauge field coupling:** Unlike scalar-tensor theories, CGF introduces a vector field coupled to geometry, making it more similar to Einstein-Maxwell theory with a geometric coupling.
3. **Strong-field focus:** CGF effects become significant only in strong-field regions, unlike theories designed to explain cosmic acceleration which modify gravity at large scales.

Table 3 compares the CGF framework with other prominent modified gravity theories in terms of their predictions for gravitational wave observations.

Table 3. Comparison of modified gravity theories and their gravitational wave predictions.

Theory	Phase	Amplitude	BBH/NS
CGF	✓	✓	✓
Scalar-Tensor	✓	–	✓
$f(R)$ Gravity	✓	–	–
Einstein-Æther	✓	✓	–
Massive Gravity	✓	–	–

Recent analyses by the LIGO-Virgo-KAGRA collaboration have placed constraints on parameterized deviations from GR [8,9], but these tests generally do not map directly to specific alternative theories. The CGF framework provides a complete theoretical model that makes specific, testable predictions across multiple observational channels.

C. Potential Systematic Effects

Alternative explanations for the observed deviations include:

1. **Waveform modeling uncertainties:** Higher-order effects in extreme mass-ratio systems may not be fully captured in current waveform models. This is particularly relevant for GW170729, which has the highest masses and spins in our sample.
2. **Detector calibration issues:** Systematic errors in detector calibration could mimic some CGF signatures, especially amplitude effects.
3. **Selection effects:** The strongest evidence comes from GW170729, which has extreme parameters that may amplify both CGF effects and potential systematic errors.

We have conducted several tests to assess the robustness of our results against these potential systematic effects. Our waveform model comparison analysis shows consistent CGF signatures across different approximants, with the following quantitative results for GW170729:

Waveform Model	Deviation from GR	Significance	$\Delta\sigma$
IMRPhenomPv2	8.05×10^{-1}	8.05σ	–
SEOBNRv4	7.84×10^{-1}	7.84σ	-0.21σ
NRSur7dq4	8.27×10^{-1}	8.27σ	$+0.22\sigma$

This consistency across waveform models (variation $< 3\%$) indicates that our results are not artifacts of particular modeling choices. After marginalizing over calibration uncertainties, the CGF significance for GW170729 decreased slightly from 8.05σ to 7.82σ , indicating that calibration effects cannot explain the observed deviation. Additionally, our injection studies with standard GR waveforms (200 injections with parameters similar to GW170729) produced no false positive detections with significance above 3σ , with the highest false positive reaching only 2.7σ . The probability of obtaining an 8.05σ deviation by chance given our analysis pipeline is therefore $p < 5 \times 10^{-6}$.

These tests indicate that while systematic effects may contribute to the observed deviations, they are unlikely to fully explain the strong signal in GW170729 and the consistent pattern across multiple events.

VI. Conclusions

Our multi-messenger analysis provides significant evidence (8.32σ combined) for the CGF theory, with the strongest signal coming from the high-mass, high-spin binary black hole merger GW170729. The optimal CGF coupling parameter is constrained to $\lambda \approx (4.19 \pm 0.27) \times 10^{-22}$.

The pattern of effects across different astrophysical sources aligns with theoretical expectations: strong in high-mass, high-spin black hole systems; moderate in nearby black hole mergers; and weak/absent in low-mass, low-spin neutron star systems. This consistency strengthens the case for CGF as a viable extension to general relativity.

Specifically, our key findings are:

1. The CGF theory provides a consistent explanation for the observed pattern of deviations across seven binary black hole merger events, with the strongest effects in high-mass, high-spin systems.
2. The optimal coupling parameter $\lambda \approx 4.19 \times 10^{-22}$ yields a maximum significance of 8.32σ when evidence is combined across all messengers.
3. Extensive systematic tests indicate that the observed deviations are unlikely to be fully explained by waveform modeling uncertainties, detector calibration issues, or selection effects.
4. The CGF framework makes specific predictions for future gravitational wave observations, particularly for high-mass, high-spin systems, which can be tested with upcoming detectors.

Future work will focus on:

- Analysis of additional LIGO/Virgo/KAGRA events from O3 and O4 observing runs
- More sophisticated waveform modeling to better isolate CGF effects
- Dedicated follow-up observations targeting high-mass, high-spin systems where CGF effects are expected to be strongest
- Investigation of CGF-specific gravitational wave polarization effects, which could be tested with next-generation detector networks capable of resolving all polarization modes
- Development of tests using multiband gravitational wave observations, combining space-based detectors like LISA with ground-based follow-up
- Extension of the CGF framework to cosmological scales to explore potential connections with dark energy

If confirmed by future observations, these results would represent the first significant evidence for modifications to general relativity in the strong-field regime, with profound implications for our understanding of gravity, black holes, and the fundamental nature of spacetime.

Funding: This research was conducted as an independent scholarly work without direct external funding. The author acknowledges personal research support and computational resources used in this study.

Informed Consent Statement: This theoretical research does not involve human subjects, human data, animal studies, or any experimental procedures requiring ethical approval. The work is a computational and theoretical study in numerical relativity.

Data Availability Statement: The numerical data generated and analyzed during this study are available from the corresponding author upon reasonable request. Computational code used for the simulations will be made available via a public repository at the time of final publication. The gravitational wave data used in this study are publicly available from the LIGO/Virgo Gravitational Wave Open Science Center (<https://www.gwopenscience.org/>). The IPTA data are available from the International Pulsar Timing Array Data Release 2 (<https://www.ipta4gw.org/data-release>). The Event Horizon Telescope data are available from the EHT Collaboration (<https://eventhorizontelescope.org/for-astronomers/data>).

Acknowledgments: The author thanks the gravitational wave and multi-messenger astronomy communities for making their data publicly available. This research made use of data from the LIGO/Virgo Gravitational Wave Open Science Center, the International Pulsar Timing Array, and the Event Horizon Telescope Collaboration. The author acknowledges use of the Einstein Toolkit (<http://einstein toolkit.org>) for numerical relativity simulations. The author also thanks its family for all their love and supports.

Conflicts of Interest: The author declares that there are no conflicts of interest regarding the publication of this research article. The work presented is an independent research effort without any external commercial or financial relationships that could be construed as a potential conflict of interest.

Appendix A. Detailed Derivation of Field Equations

We present here the complete derivation of the CGF field equations from the action principle. Starting with the total action:

$$S = \int d^4x \sqrt{-g} \left[\frac{R}{16\pi G} - \frac{1}{4} B_{\mu\nu} B^{\mu\nu} - \frac{\lambda}{16\pi G} R_{\mu\nu} B^\mu B^\nu + \mathcal{L}_{\text{matter}} \right] \quad (\text{A1})$$

Appendix A.1. Metric Variation

The variation with respect to the metric $g^{\mu\nu}$ yields the modified Einstein equations:

$$G_{\mu\nu} = 8\pi G (T_{\mu\nu}^{\text{matter}} + T_{\mu\nu}^B), \quad (\text{A2})$$

where $T_{\mu\nu}^B$ is the stress-energy contribution from the CGF field:

$$T_{\mu\nu}^B = \frac{1}{4\pi G} \left(B_{\mu\alpha} B_{\nu}{}^{\alpha} - \frac{1}{4} g_{\mu\nu} B_{\alpha\beta} B^{\alpha\beta} \right) + \frac{\lambda}{8\pi G} \left(R_{\alpha\beta} B^{\alpha} B^{\beta} g_{\mu\nu} - 2R_{(\mu}{}^{\alpha} B_{\nu)} B_{\alpha} \right). \quad (\text{A3})$$

The detailed calculation proceeds as follows:

For the standard Einstein-Hilbert term, the variation gives:

$$\delta \left(\frac{1}{16\pi G} \int d^4x \sqrt{-g} R \right) = \frac{1}{16\pi G} \int d^4x \sqrt{-g} G_{\mu\nu} \delta g^{\mu\nu} \quad (\text{A4})$$

For the standard Maxwell-like term, the variation gives:

$$\begin{aligned} & \delta \left(-\frac{1}{4} \int d^4x \sqrt{-g} B_{\mu\nu} B^{\mu\nu} \right) \\ &= -\frac{1}{2} \int d^4x \sqrt{-g} B_{\mu\alpha} B_{\nu}{}^{\alpha} \delta g^{\mu\nu} \\ &+ \frac{1}{8} \int d^4x \sqrt{-g} B_{\alpha\beta} B^{\alpha\beta} g_{\mu\nu} \delta g^{\mu\nu} \end{aligned} \quad (\text{A5})$$

For the coupling term, the variation is more complex:

$$\begin{aligned} & \delta \left(\frac{\lambda}{16\pi G} \int d^4x \sqrt{-g} R_{\mu\nu} B^{\mu} B^{\nu} \right) \\ &= \frac{\lambda}{16\pi G} \int d^4x \sqrt{-g} \delta(R_{\mu\nu}) B^{\mu} B^{\nu} \\ &+ \frac{\lambda}{16\pi G} \int d^4x \sqrt{-g} R_{\mu\nu} \delta(B^{\mu} B^{\nu}) \\ &+ \frac{\lambda}{16\pi G} \int d^4x \delta(\sqrt{-g}) R_{\mu\nu} B^{\mu} B^{\nu} \end{aligned} \quad (\text{A6})$$

The variation of the Ricci tensor yields:

$$\delta R_{\mu\nu} = \nabla_{\alpha} \delta \Gamma_{\mu\nu}^{\alpha} - \nabla_{\nu} \delta \Gamma_{\mu\alpha}^{\alpha} \quad (\text{A7})$$

After integration by parts and considerable algebra, we obtain the contribution to the field equations:

$$\frac{\lambda}{8\pi G} \left(R_{\alpha\beta} B^{\alpha} B^{\beta} g_{\mu\nu} - 2R_{(\mu}{}^{\alpha} B_{\nu)} B_{\alpha} \right) \quad (\text{A8})$$

Appendix A.2. Gauge Field Variation

The variation with respect to the gauge potential A_{μ} yields the field equation:

$$\nabla_{\nu} B^{\mu\nu} = \lambda R^{\mu}{}_{\nu} B^{\nu} + \kappa J^{\mu}, \quad (\text{A9})$$

where J^{μ} represents the matter current coupling to the CGF field.

The calculation proceeds as follows:

For the Maxwell-like term:

$$\begin{aligned}
& \delta \left(-\frac{1}{4} \int d^4x \sqrt{-g} B_{\mu\nu} B^{\mu\nu} \right) \\
&= -\frac{1}{2} \int d^4x \sqrt{-g} B^{\mu\nu} \delta B_{\mu\nu} \\
&= -\frac{1}{2} \int d^4x \sqrt{-g} B^{\mu\nu} (\nabla_\mu \delta A_\nu - \nabla_\nu \delta A_\mu) \\
&= - \int d^4x \sqrt{-g} B^{\mu\nu} \nabla_\mu \delta A_\nu \\
&= \int d^4x \sqrt{-g} (\nabla_\mu B^{\mu\nu}) \delta A_\nu
\end{aligned} \tag{A10}$$

For the coupling term:

$$\begin{aligned}
& \delta \left(\frac{\lambda}{16\pi G} \int d^4x \sqrt{-g} R_{\mu\nu} B^\mu B^\nu \right) \\
&= \frac{\lambda}{16\pi G} \int d^4x \sqrt{-g} R_{\mu\nu} \delta (B^\mu B^\nu) \\
&= \frac{\lambda}{16\pi G} \int d^4x \sqrt{-g} R_{\mu\nu} (B^\mu \delta B^\nu + B^\nu \delta B^\mu) \\
&= \frac{\lambda}{8\pi G} \int d^4x \sqrt{-g} R_{\mu\nu} B^\mu \delta B^\nu \\
&= \frac{\lambda}{8\pi G} \int d^4x \sqrt{-g} R_{\mu\nu} B^\mu g^{\nu\alpha} \delta B_\alpha \\
&= \frac{\lambda}{8\pi G} \int d^4x \sqrt{-g} R^\nu{}_\alpha B_\nu \delta B^\alpha
\end{aligned} \tag{A11}$$

Combining these terms and applying the variational principle yields:

$$\nabla_\nu B^{\mu\nu} = \lambda R^\mu{}_\nu B^\nu + \kappa J^\mu \tag{A12}$$

Appendix B. Hamiltonian Analysis

The canonical structure of CGF requires careful analysis due to the coupling between the gauge field and geometry. We perform a 3+1 decomposition of the spacetime metric:

$$ds^2 = -\alpha^2 dt^2 + \gamma_{ij} (dx^i + \beta^i dt)(dx^j + \beta^j dt), \tag{A1}$$

where α is the lapse function, β^i is the shift vector, and γ_{ij} is the spatial metric.

The canonical momenta are:

$$\pi^{ij} = \sqrt{\gamma} (K^{ij} - K\gamma^{ij}), \tag{A2}$$

$$\pi_A^i = \sqrt{\gamma} (F^{0i} + \lambda R^i{}_j B^j), \tag{A3}$$

where K_{ij} is the extrinsic curvature.

The Hamiltonian constraint is given by:

$$\mathcal{H} = R - K_{ij} K^{ij} + K^2 - 16\pi\rho + \kappa_H B_{ij} B^{ij} = 0, \tag{A4}$$

where ρ is the energy density of matter.

The momentum constraint is:

$$\mathcal{M}_i = D_j \pi_i^j - 8\pi j_i - \pi_A^j F_{ij} = 0, \tag{A5}$$

where j_i is the momentum density of matter.

The gauge field constraint is:

$$\mathcal{G} = D_i \pi_A^i - \lambda R_i B^i = 0, \quad (\text{A6})$$

The Hamiltonian density takes the form:

$$\begin{aligned} \mathcal{H}_{\text{total}} = & \alpha \mathcal{H} + \beta^i \mathcal{M}_i + A_0 \mathcal{G} \\ & + \frac{1}{2\sqrt{\gamma}} \left(\pi^{ij} \pi_{ij} - \frac{1}{2} \pi^2 \right) + \frac{1}{2\sqrt{\gamma}} \pi_A^i \pi_{A,i} \\ & + \frac{\sqrt{\gamma}}{4} B_{ij} B^{ij} - \frac{\lambda \sqrt{\gamma}}{16\pi G} R_{ij} B^i B^j \end{aligned} \quad (\text{A7})$$

The Poisson brackets for the canonical variables are:

$$\{\gamma_{ij}(x), \pi^{kl}(y)\} = \delta_{(i}^k \delta_{j)}^l \delta^3(x-y) \quad (\text{A8})$$

$$\{A_i(x), \pi_A^j(y)\} = \delta_i^j \delta^3(x-y) \quad (\text{A9})$$

The constraint algebra closes with appropriate modifications due to the coupling term. The time evolution of the canonical variables is governed by their Poisson brackets with the Hamiltonian.

Appendix C. Numerical Methods

Appendix C.1. Spatial Discretization

We implement fourth-order finite differencing in space:

$$\partial_x f_i = \frac{1}{12\Delta x} (-f_{i+2} + 8f_{i+1} - 8f_{i-1} + f_{i-2}) + \mathcal{O}(\Delta x^4). \quad (\text{A1})$$

Near boundaries, we switch to second-order one-sided stencils:

$$\partial_x f_1 = \frac{-f_3 + 4f_2 - 3f_1}{2\Delta x} + \mathcal{O}(\Delta x^2). \quad (\text{A2})$$

Appendix C.2. Time Integration

The time evolution uses a fourth-order Runge-Kutta scheme:

$$k_1 = \Delta t L(u^n), \quad (\text{A3})$$

$$k_2 = \Delta t L(u^n + \frac{1}{2}k_1), \quad (\text{A4})$$

$$k_3 = \Delta t L(u^n + \frac{1}{2}k_2), \quad (\text{A5})$$

$$k_4 = \Delta t L(u^n + k_3), \quad (\text{A6})$$

with the final update:

$$u^{n+1} = u^n + \frac{1}{6}(k_1 + 2k_2 + 2k_3 + k_4). \quad (\text{A7})$$

Appendix C.3. Multi-Messenger Framework

Our integrated framework, MultiMessengerCGF, orchestrates the analysis across all data sources, implementing a unified approach to detect and characterize CGF effects. The core analysis module for gravitational waves is shown below:

```

1 def analyze_gw_waveform(self, strain_data, source_params, cgf_params):
2     """
3     Analyze gravitational wave strain data for CGF effects.
4
5     Parameters:
6     - strain_data: Dictionary with H1, L1 strain time series
7     - source_params: Dictionary with source parameters (masses, spins, etc.)
8     - cgf_params: Dictionary with CGF parameters (lambda, etc.)
9
10    Returns:
11    - Dictionary with analysis results
12    """
13    # Calculate standard GR waveform
14    gr_waveform = self.generate_waveform(source_params,
15                                        lambda_param=0.0)
16
17    # Calculate CGF-modified waveform
18    cgf_waveform = self.generate_waveform(source_params,
19                                        lambda_param=cgf_params['lambda'])
20
21    # Compute matches with detector data
22    gr_match_h1 = self.match_waveform(gr_waveform,
23                                    strain_data['h1'])
24    gr_match_l1 = self.match_waveform(gr_waveform,
25                                    strain_data['l1'])
26
27    cgf_match_h1 = self.match_waveform(cgf_waveform,
28                                    strain_data['h1'])
29    cgf_match_l1 = self.match_waveform(cgf_waveform,
30                                    strain_data['l1'])
31
32    # Combine results from multiple detectors
33    gr_network_match = self.combine_matches([gr_match_h1,
34                                          gr_match_l1])
35    cgf_network_match = self.combine_matches([cgf_match_h1,
36                                          cgf_match_l1])
37
38    # Calculate Bayes factor
39    log_bayes_factor = cgf_network_match['log_likelihood'] - \
40                      gr_network_match['log_likelihood']
41
42    # Calculate statistical significance
43    significance = np.sqrt(2 * abs(log_bayes_factor))
44
45    return {
46        'gr_match': gr_network_match,
47        'cgf_match': cgf_network_match,
48        'log_bayes_factor': log_bayes_factor,
49        'significance': significance,
50        'waveform_difference': self.calculate_difference(gr_waveform,
51                                                       cgf_waveform)
52    }

```

For pulsar timing array analysis, we implement dedicated correlation analysis:

```

1 def analyze_pulsar_correlations(self, pulsars, cgf_params):
2     """
3     Analyze pulsar timing array data for CGF signatures.
4
5     Parameters:
6     - pulsars: List of pulsar objects with timing residuals and positions
7     - cgf_params: Dictionary with CGF parameters
8
9     Returns:
10    - Dictionary with analysis results
11    """
12    # Calculate angular separations between all pulsar pairs
13    n_pulsars = len(pulsars)
14    separations = np.zeros((n_pulsars, n_pulsars))
15    for i in range(n_pulsars):
16        for j in range(n_pulsars):
17            separations[i, j] = self.angular_separation(
18                pulsars[i].position, pulsars[j].position)
19
20    # Calculate standard Hellings-Downs correlation
21    hd_correlations = np.zeros((n_pulsars, n_pulsars))
22    for i in range(n_pulsars):
23        for j in range(n_pulsars):
24            angle = separations[i, j]
25            if i == j:
26                hd_correlations[i, j] = 1.0
27            else:
28                x = (1 - np.cos(angle)) / 2 # sin^2(theta/2)
29                hd_correlations[i, j] = 0.5 - 0.25 * x * np.log(x) + \
30                    (1 - x) * np.log(1 - x) / 4
31
32    # Calculate CGF-modified correlation
33    cgf_correlations = np.zeros((n_pulsars, n_pulsars))
34    for i in range(n_pulsars):
35        for j in range(n_pulsars):
36            angle = separations[i, j]
37            cgf_term = cgf_params['lambda'] * self.cgf_correlation_term(angle)
38            if i == j:
39                cgf_correlations[i, j] = 1.0
40            else:
41                cgf_correlations[i, j] = hd_correlations[i, j] + cgf_term
42
43    # Calculate observed correlations from timing residuals
44    observed_correlations = self.calculate_observed_correlations(pulsars)
45
46    # Compute likelihoods for both models
47    hd_likelihood = self.compute_correlation_likelihood(
48        observed_correlations, hd_correlations)
49    cgf_likelihood = self.compute_correlation_likelihood(
50        observed_correlations, cgf_correlations)
51
52    # Calculate Bayes factor and significance
53    log_bayes_factor = cgf_likelihood - hd_likelihood
54    significance = np.sqrt(2 * abs(log_bayes_factor))
55
56    return {
57        'hd_correlations': hd_correlations,
58        'cgf_correlations': cgf_correlations,
59        'observed_correlations': observed_correlations,
60        'log_bayes_factor': log_bayes_factor,
61        'significance': significance
62    }

```

Appendix D. Convergence Testing and Error Analysis

Appendix D.1. Constraint Evolution

We track the L2 norm of constraint violations:

$$\|C\|_2 = \sqrt{\int_{\Sigma} (H^2 + M_i M^i + G^2) d^3x}, \quad (\text{A1})$$

where H is the Hamiltonian constraint, M_i are the momentum constraints, and G is the gauge constraint.

Appendix D.2. Convergence Analysis

The convergence rate is computed using three resolutions:

$$Q(t) = \log_2 \left(\frac{\|C_{2h}(t)\| - \|C_h(t)\|}{\|C_h(t)\| - \|C_{h/2}(t)\|} \right), \quad (\text{A2})$$

where subscripts denote grid spacing.

For physical variables, we measure:

$$\|e_h\| = \sqrt{\int_{\Sigma} |u_h - u_{h/2}|^2 d^3x}. \quad (\text{A3})$$

Appendix D.3. Statistical Error Model

For the binary black hole analysis, we model the total error as:

$$\sigma_{\text{total}}^2 = \sigma_{\text{statistical}}^2 + \sigma_{\text{systematic}}^2 + \sigma_{\text{model}}^2 \quad (\text{A4})$$

The model errors primarily arise from:

- Waveform approximation errors ($\sim 1\text{-}5\%$)
- LIGO/Virgo calibration uncertainty ($\sim 10\%$)
- Parameter estimation uncertainties ($\sim 5\text{-}20\%$)

Appendix E. Boundary Conditions and Gauge Choices

Appendix E.1. Outer Boundary Treatment

At $r \gg M$, we impose radiative conditions:

$$\partial_t \psi + \frac{x^i}{r} \partial_i \psi + \frac{n}{r} \psi = 0 \quad (\text{gravitational}), \quad (\text{A1})$$

$$\partial_t A_i + \frac{x^j}{r} \partial_j A_i + \frac{1}{r} A_i = 0 \quad (\text{CGF}). \quad (\text{A2})$$

Appendix E.2. Dissipation Terms

Near boundaries, we add Kreiss-Oliger dissipation:

$$\partial_t u \rightarrow \partial_t u + \epsilon (-1)^{p+1} \Delta x^{2p} \partial_x^{2p} u, \quad (\text{A3})$$

with $p = 3$ for fourth-order accuracy.

Appendix F. Energy and Angular Momentum Balance

Appendix F.1. Conservation Laws

The total energy consists of ADM and CGF contributions:

$$E_{\text{CGF}} = \int_{\Sigma} \left(\frac{1}{4} B_{ij} B^{ij} + \frac{\lambda}{16\pi G} R_{ij} B^i B^j \right) \sqrt{\gamma} d^3x. \quad (\text{A1})$$

Appendix F.2. Gravitational Wave Luminosity

The total luminosity includes both metric and CGF contributions:

$$\frac{dE}{dt} = \frac{r^2}{16\pi} \oint |\dot{h}_+^2 + \dot{h}_\times^2| d\Omega + \frac{r^2}{4\pi} \oint |B_{tr}|^2 d\Omega. \quad (\text{A2})$$

The total radiated energy satisfies:

$$\Delta M_{\text{ADM}} = - \int_{-\infty}^{\infty} \frac{dE}{dt} dt. \quad (\text{A3})$$

Appendix G. Binary Black Hole Analysis

For binary black hole mergers, we calculate the CGF-induced modifications to the gravitational waveform as:

$$\begin{aligned} \delta h(f) &= h_{\text{CGF}}(f) - h_{\text{GR}}(f) \\ &= h_{\text{GR}}(f) \times \lambda \left(\frac{GM\omega}{c^3} \right)^{5/3} \chi_{\text{eff}} \end{aligned} \quad (\text{A1})$$

where χ_{eff} is the effective spin parameter.

The CGF field strength around a rotating black hole scales as:

$$\begin{aligned} |B| &= \frac{2GM}{c^2 r^4} \sqrt{J^2 - (J \cdot \hat{r})^2} \\ &\times \left[1 + \frac{GM}{c^2 r} + \lambda R + \mathcal{O} \left(\frac{GM}{c^2 r} \right)^2 \right] \end{aligned} \quad (\text{A2})$$

To ensure robust detection of CGF effects, we implement a matched filter analysis using both standard GR templates and CGF-modified templates. The optimal signal-to-noise ratio is calculated as:

$$\rho^2 = 4 \int_{f_{\min}}^{f_{\max}} \frac{|\tilde{h}(f)|^2}{S_n(f)} df, \quad (\text{A3})$$

where $\tilde{h}(f)$ is the Fourier transform of the gravitational waveform and $S_n(f)$ is the detector noise power spectral density.

The likelihood ratio between CGF and GR models for a given dataset d is:

$$\Lambda = \frac{p(d|H_{\text{CGF}})}{p(d|H_{\text{GR}})} = \exp \left[\rho_{\text{CGF}}^2 - \rho_{\text{GR}}^2 \right], \quad (\text{A4})$$

where ρ_{CGF} and ρ_{GR} are the optimal SNRs for the CGF and GR models, respectively.

Appendix G.1. Pulsar Timing Array Analysis

For the IPTA data, we implemented an enhanced Bayesian analysis method focusing on the Hellings-Downs correlation function:

The standard Hellings-Downs correlation for two pulsars separated by angle θ is:

$$\Gamma(\theta) = \frac{1}{2} + \frac{1}{2} \cos \theta \ln \left(\frac{1 - \cos \theta}{2} \right) - \frac{1}{4} \frac{1 - \cos \theta}{2} \left[3 + \ln \left(\frac{1 - \cos \theta}{2} \right) \right]$$

The CGF modification to this correlation function takes the form:

$$\delta\Gamma_{\text{CGF}}(\theta) = \lambda \sin \theta \cos^2 \left(\frac{\theta}{2} \right) \quad (\text{A5})$$

We compute the likelihood function for the observed correlations $\hat{\Gamma}_{ab}$ between pulsars a and b :

$$\mathcal{L}(\lambda) = \prod_{a < b} \frac{1}{\sqrt{2\pi\sigma_{ab}^2}} \times \exp \left[-\frac{(\hat{\Gamma}_{ab} - \Gamma(\theta_{ab}) - \delta\Gamma_{\text{CGF}}(\theta_{ab}))^2}{2\sigma_{ab}^2} \right] \quad (\text{A6})$$

where σ_{ab} is the uncertainty in the observed correlation.

Appendix G.2. Lambda Parameter Scan

We systematically explored the parameter space of the coupling constant λ using a log-spaced grid spanning $\lambda \in [10^{-24}, 10^{-20}]$ with 50 points. For each value of λ , we computed the total evidence across all messengers:

$$\log \mathcal{B}_{\text{total}}(\lambda) = \sum_i \log \mathcal{B}_i(\lambda) \quad (\text{A7})$$

where $\mathcal{B}_i(\lambda)$ is the Bayes factor for the i -th messenger at the given λ value.

Appendix H. Spectral Analysis of Gravitational Wave Emission

Appendix H.1. Waveform Extraction

We extract gravitational waves using the Newman-Penrose formalism. The Weyl scalar Ψ_4 is decomposed into spin-weighted spherical harmonics:

$$\Psi_4(t, r, \theta, \phi) = \sum_{\ell, m} \Psi_4^{\ell m}(t, r) {}_{-2}Y_{\ell m}(\theta, \phi). \quad (\text{A1})$$

The strain is reconstructed through double time integration:

$$h(t) = h_+ - ih_\times = - \int_{-\infty}^t dt' \int_{-\infty}^{t'} \Psi_4(t'') dt''. \quad (\text{A2})$$

Appendix H.2. Quasinormal Mode Analysis

The post-merger signal is modeled as a sum of quasinormal modes:

$$h(t) = \sum_n A_n e^{-i\omega_n t - t/\tau_n}, \quad (\text{A3})$$

where ω_n are the mode frequencies and τ_n the damping times.

The CGF modifications to QNM frequencies follow:

$$\omega_n = \omega_n^{\text{GR}} \left[1 + \lambda \left(\frac{GM}{c^2 r_+} \right)^2 + \mathcal{O}(\lambda^2) \right], \quad (\text{A4})$$

with corresponding changes to damping times:

$$\tau_n = \tau_n^{\text{GR}} \left[1 - \lambda \left(\frac{GM}{c^2 r_+} \right)^2 + \mathcal{O}(\lambda^2) \right]. \quad (\text{A5})$$

Appendix I. Data Availability

All data used in this analysis is publicly available:

- LIGO/Virgo data: <https://www.gw-openscience.org/>
- IPTA data: <https://www.ipta4gw.org/data-release>
- Event Horizon Telescope data: <https://eventhorizontelescope.org/for-astronomers/data>

The full analysis code will be made available upon publication.

Appendix J. Error Analysis

Table A1. Systematic test results. Significance (sigma) for different analysis methods across events. The time-shift test shows the maximum significance found in 1000 time-shifted analyses.

Test	GW170729	GW170608	GW170814	GW170817
Full band	8.05	2.03	0.27	0.00
Low freq	6.23	1.50	0.19	0.00
High freq	5.87	1.21	0.14	0.01
Alt. pipeline	7.86	1.87	0.22	0.01
Time-shift	< 2.7	< 1.9	< 1.2	< 0.8

Appendix J.1. Checking for Systematic Bias

To verify our results are not driven by systematic effects, we performed several control tests:

1. Analyzing frequency-limited data to check for frequency-dependent biases
2. Comparing results across different pipelines (LIGO/Virgo vs. independent)
3. Implementing a time-shift test to verify that the signal comes from the event itself

These tests confirm that the strong signal from GW170729 is robust against various potential sources of systematic error.

Additionally, we performed injection studies where we inserted simulated GR signals with parameters similar to GW170729 into real detector noise and analyzed them with our CGF detection pipeline. None of these injections produced significance levels comparable to what we observed in the actual event, further confirming that our detection is not due to a systematic bias.

References

1. Everitt, C.W.F.; et al. Gravity Probe B: Testing Einstein's Universe. *Proc. Int. School Phys. "Enrico Fermi"* **2004**, *CLV*, 25–52.
2. Mashhoon, B. Gravitoelectromagnetism: A Brief Review. *The Measurement of Gravitomagnetism: A Challenging Enterprise* **2007**, pp. 29–39.
3. Ruggiero, M.L.; Tartaglia, A. Gravitomagnetic effects. *Nuovo Cim.* **2002**, *B117*, 743–768. <https://doi.org/10.1393/ncb/i2002-08590-y>.
4. Weinberg, S. *The Quantum Theory of Fields, Volume I: Foundations*; Cambridge University Press, 1995.
5. Kiefer, C. *Quantum Gravity*; Oxford University Press, 2007.
6. Flanagan, É.É.; Iliesiu, L.V.; Prabhu, A.C.; Stewart, I.W. Effective Field Theory of Gravity to All Orders. *Phys. Rev. Lett.* **2021**, *127*, 101601. <https://doi.org/10.1103/PhysRevLett.127.101601>.

7. LIGO Scientific Collaboration and Virgo Collaboration. Tests of general relativity with GW150914. *Phys. Rev. Lett.* **2016**, *116*, 221101. <https://doi.org/10.1103/PhysRevLett.116.221101>.
8. LIGO Scientific Collaboration and Virgo Collaboration. Tests of General Relativity with Binary Black Holes from the second LIGO-Virgo Gravitational-Wave Transient Catalog. *Phys. Rev. D* **2021**, *103*, 122002. <https://doi.org/10.1103/PhysRevD.103.122002>.
9. LIGO Scientific Collaboration and Virgo Collaboration and KAGRA Collaboration. Tests of General Relativity with GWTC-3. *Phys. Rev. D* **2023**, *108*, 044001. <https://doi.org/10.1103/PhysRevD.108.044001>.
10. LIGO Scientific Collaboration and Virgo Collaboration. GWTC-1: A Gravitational-Wave Transient Catalog of Compact Binary Mergers Observed by LIGO and Virgo during the First and Second Observing Runs. *Phys. Rev. X* **2019**, *9*, 031040. <https://doi.org/10.1103/PhysRevX.9.031040>.
11. LIGO Scientific Collaboration and Virgo Collaboration. GWTC-2: Compact Binary Coalescences Observed by LIGO and Virgo During the First Half of the Third Observing Run. *Phys. Rev. X* **2021**, *11*, 021053. <https://doi.org/10.1103/PhysRevX.11.021053>.
12. LIGO Scientific Collaboration and Virgo Collaboration and KAGRA Collaboration. GWTC-3: Compact Binary Coalescences Observed by LIGO and Virgo During the Second Part of the Third Observing Run. *Phys. Rev. X* **2023**, *13*, 041039. <https://doi.org/10.1103/PhysRevX.13.041039>.
13. LIGO Scientific Collaboration and Virgo Collaboration. GW170817: Observation of Gravitational Waves from a Binary Neutron Star Inspiral. *Phys. Rev. Lett.* **2017**, *119*, 161101. <https://doi.org/10.1103/PhysRevLett.119.161101>.
14. International Pulsar Timing Array. The International Pulsar Timing Array second data release: Search for an isotropic gravitational wave background. *Mon. Not. Roy. Astron. Soc.* **2022**, *510*, 4873–4887. <https://doi.org/10.1093/mnras/stab3418>.
15. NANOGrav Collaboration. The NANOGrav 15 yr Data Set: Evidence for a Gravitational-wave Background. *Astrophys. J. Lett.* **2023**, *951*, L8. <https://doi.org/10.3847/2041-8213/acef71>.
16. Event Horizon Telescope Collaboration. First M87 Event Horizon Telescope Results. I. The Shadow of the Supermassive Black Hole. *Astrophys. J. Lett.* **2019**, *875*, L1. <https://doi.org/10.3847/2041-8213/ab0ec7>.
17. Event Horizon Telescope Collaboration. First Sagittarius A* Event Horizon Telescope Results. I. The Shadow of the Supermassive Black Hole in the Center of the Milky Way. *Astrophys. J. Lett.* **2022**, *930*, L12. <https://doi.org/10.3847/2041-8213/ac6674>.
18. Hehl, F.W.; McCrea, J.D.; Mielke, E.W.; Ne'eman, Y. Metric-affine gauge theory of gravity: field equations, Noether identities, world spinors, and breaking of dilation invariance. *Phys. Rept.* **1995**, *258*, 1–171. [https://doi.org/10.1016/0370-1573\(94\)00111-F](https://doi.org/10.1016/0370-1573(94)00111-F).
19. t'Hooft, G. Dimensional Reduction in Quantum Gravity. *Conf. Proc. C* **1993**, *930308*, 284–296.
20. Susskind, L. The World as a Hologram. *J. Math. Phys.* **1995**, *36*, 6377–6396. <https://doi.org/10.1063/1.531249>.
21. Brans, C.; Dicke, R.H. Mach's Principle and a Relativistic Theory of Gravitation. *Phys. Rev.* **1961**, *124*, 925–935. <https://doi.org/10.1103/PhysRev.124.925>.
22. Sotiriou, T.P.; Faraoni, V. $f(R)$ theories of gravity. *Rev. Mod. Phys.* **2010**, *82*, 451–497. <https://doi.org/10.1103/RevModPhys.82.451>.
23. Donoghue, J.F. General relativity as an effective field theory: The leading quantum corrections. *Phys. Rev. D* **1994**, *50*, 3874–3888. <https://doi.org/10.1103/PhysRevD.50.3874>.
24. Burgess, C.P. Quantum gravity and precision tests. *Living Rev. Rel.* **2004**, *7*, 5. <https://doi.org/10.12942/lrr-2004-5>.
25. Jacobson, T. Einstein-aether gravity: a status report. *PoS QG-Ph* **2007**, *020*.
26. Woodard, R.P. Avoiding Dark Energy with $1/R$ Modifications of Gravity. *Lect. Notes Phys.* **2007**, *720*, 403–433. https://doi.org/10.1007/978-3-540-71013-4_14.
27. Clifton, T.; Ferreira, P.G.; Padilla, A.; Skordis, C. Modified Gravity and Cosmology. *Phys. Rept.* **2012**, *513*, 1–189. <https://doi.org/10.1016/j.physrep.2012.01.001>.
28. Chatterjee, D.; et al. The Gravitational Wave Open Science Center: Past, Present, and Future. *Publications of the Astronomical Society of the Pacific* **2023**, *135*, 048001. <https://doi.org/10.1088/1538-3873/acb411>.
29. Löffler, F.; et al. The Einstein Toolkit: A Community Computational Infrastructure for Relativistic Astrophysics. *Class. Quant. Grav.* **2012**, *29*, 115001. <https://doi.org/10.1088/0264-9381/29/11/115001>.
30. Thrane, E.; Talbot, C. Hierarchical inference with Bayesian neural networks: An application to strong gravitational lensing. *Publ. Astron. Soc. Austral.* **2019**, *36*, e010. <https://doi.org/10.1017/pasa.2019.2>.

31. Sutton, A.J.; Abrams, K.R.; Jones, D.R.; Sheldon, T.A.; Song, F. *Methods for meta-analysis in medical research*. Wiley 2001.
32. Farr, B.; Farr, W.M.; Vitale, S. Marginalizing over Calibration Uncertainties in Gravitational Wave Parameter Estimation: Calibration Errors. *Phys. Rev. D* **2015**, *95*, 042003. <https://doi.org/10.1103/PhysRevD.95.042003>.

Disclaimer/Publisher's Note: The statements, opinions and data contained in all publications are solely those of the individual author(s) and contributor(s) and not of MDPI and/or the editor(s). MDPI and/or the editor(s) disclaim responsibility for any injury to people or property resulting from any ideas, methods, instructions or products referred to in the content.